RF-quantum capacitance of topological insulator Bi_2Se_3 in the bulk depleted regime

A. Inhofer[1], J. Duffy[2,3], M. Boukhicha[1], E. Bocquillon[1], J. Palomo[2], K. Watanabe[4], T. Taniguchi[4], I. Estève[5], J.M. Berroir[1], G. Fève[1], B. Plaçais[1], B.A. Assaf[2]

[1] *Laboratoire Pierre Aigrain, Ecole Normale Supérieure, CNRS, PSL Research University, Université Pierre et Marie Curie, Sorbonne Universités, Université Denis Diderot, Sorbonne Cité, 24 rue Lhomond, 75005 Paris, France*

[2] *Département de Physique, Ecole Normale Supérieure, CNRS, PSL Research University, 24 rue Lhomond, 75005 Paris, France*

[3] *Chemical Engineering Department, Northeastern University, 360 Huntington Avenue, Boston MA, 02115, USA*

[4] *National Institute for Materials Science, Tsukuba, Japan.*

[5] *Institut de Minéralogie, de Physique des Matériaux et de Cosmochimie, UMR 7590 CNRS UPMC-IRD-MNHN, Campus Jussieu, 4 Place Jussieu, 75005 Paris, France.*

Abstract

A Metal-dielectric-topological insulator capacitor device based on hBN-encapsulated CVD grown Bi_2Se_3 is realized and investigated in the radio frequency regime. The RF quantum capacitance and device resistance are extracted for frequencies as a high as 10 GHz, and studied as a function of applied gate voltage. The combination of the superior quality hBN dielectric gate with the optimized transport characteristics of CVD grown Bi_2Se_3 ($n\sim10^{18}cm^{-3}$ in 8 nm) allow us to attain a bulk depleted regime by dielectric gating. A quantum capacitance minimum is observed revealing a purely Dirac regime, where the Dirac surface state in proximity to the gate reaches charge neutrality, but the bottom surface Dirac cone remains charged, and couples capacitively to the top surface via the insulating bulk. Our work paves the way towards implementation of topological materials in RF devices.

Introduction

Topological phases of matter have emerged as a novel paradigm in the study of condensed matter physics.[1,2,3,4] Topological insulators are essentially material realizations that stem from this new theoretical paradigm.[4,5,6,7,8] They are interesting from both the fundamental and applied perspective. Typically, a topological insulator is a material that has an inverted orbital band ordering in the 3D bulk, which leads to existence of an odd number of Dirac cones at the 2D surface of the material, at symmetric points in the Brillouin zone.[4,5] These Dirac fermions are spin-momentum locked and highly robust to backscattering. A number of novel states of matter have so far been realized in topological insulators. The quantum anomalous Hall state,[9,10] the Majorana fermion[11] and the quantized Faraday and Kerr effects are examples of such realizations.[12,13]

Bi_2Se_3 is the prototypical topological insulator.[14,15] In this material, a single surface Dirac cone occurs at the $\overline{\Gamma}$-point of the Brillouin zone, and is well isolated from the bulk conduction and valence bands. As a result, Bi_2Se_3 has been the subject of a number of studies that use angle resolved photoemission,[16][17][18] and scanning electron microscopy.[19] Both quickly revealed signatures of the Dirac surface states. Subsequently, several studies took interest in studying DC and low frequency quantum transport,[20] either in the coherent regime,[21,22,23,24,25] or the Landau quantized regime.[16,26,27,28,29,30] The radio frequency (RF) transport regime has yet to be explored in Bi_2Se_3. This transport regime has been of significant importance in studies of graphene,[31,32,33] and more recently of HgTe TIs,[34,35] mostly when it comes to measuring the density-of-states, and determining different scattering processes that influence electron transport. Overall, the advantage of RF capacitance measurements, is that it allows one to extract simultaneously the quantum capacitance and channel resistance of materials.[31]

Reliable RF transport studies, however require the availability of materials having a low bulk carrier density and a high electron mobility. This has been successfully achieved in graphene, but remains highly challenging in Bi-based 3D-TIs. In the case of Bi_2Se_3 for example, residual bulk n-doping renders a reliable detection of surface-state signatures difficult. The first step in realizing an RF-transport device based on Bi_2Se_3 is thus a solution to this problem.

Inspired by recent work on the growth of Bi_2Se_3 by chemical vapor deposition (CVD) on mechanically exfoliated hexagonal boron nitride (hBN),[36,37] we undertake a similar procedure to grow Bi_2Se_3 on high-quality hBN,[38,39] followed by a transfer of a second layer of hBN of top of the grown Bi_2Se_3. The excellent dielectric properties of the hBN used in this work, and the improved transport characteristics of CVD grown Bi_2Se_3 on hBN, allow us to observe clear signatures of topological surface states in the RF transport regime in hBN-Bi_2Se_3-hBN heterostructures.

We report RF measurements of the quantum capacitance and the resistance in hBN-Bi_2Se_3-hBN metal-insulator-topological insulator capacitors (MITI-CAP) based on high-quality CVD Bi_2Se_3. We successfully reach a bulk depleted regime using the top gate voltage. We observe a modulation of the quantum capacitance versus gate voltage (and Fermi energy) characteristic of topological surface states (TSS) in Bi_2Se_3, exhibiting a clear capacitance minimum consistent with previous low frequency measurements. We then show that our data agree quantitatively with a model that includes top and bottom TSS contributions that are strongly capacitively coupled via the insulating bulk, the capacitance dip signaling the charge neutrality of the top surface and the background capacitance originating from an electron doped backsurface. Below the observed dip, the TI is in the bipolar regime where the top surface is *p*-type and the bottom surface is *n*-type. Finally, we extract the resistance versus gate voltage, showing a strong increase in the depleted regime. The resistance however does not reach a maximum at the capacitance dip due to the contribution of the bottom surface in the bipolar regime. Our work provides a first quantitative analysis of the compressibility of Bi_2Se_3 in the RF regime.

Methods

Bi_2Se_3 nanoflakes are grown by catalyst free chemical vapor deposition using a three zone tube furnace following a procedure similar to what is reported by Xu et al.[36] The furnace tube is initially pumped down to $8x10^{-2}$mbar. A powder source of high purity (99.99%) Bi_2Se_3 is placed in the hot zone (A) of the furnace in a stream of Argon gas (99.999%) flowing at 200 sccm, to maintain an absolute pressure of 3.9 mbar during the growth (Fig. 1(a)). A Si/SiO_2 substrate (Fig. 1(b)) on which we mechanically exfoliate high-quality hBN is placed downstream from the source in the colder zone (B). Zones (A) and (B) are initially heated up to 300^0C in 30 min. (A) then is heated up to 600^0C while (B) is only heated up to 400^0C in 30 min. These temperatures are maintained for 60 seconds. Both zones are finally cooled down to 200^0C in 80 min. The samples are then characterized using atomic force microscopy (AFM), micro-Raman spectroscopy and scanning tunneling microscopy. Selected flakes are characterized thoroughly, then covered with a top hBN-flake, to make an encapsulated hBN-Bi_2Se_3-hBN heterostructure, and finally implemented in devices.

The devices are characterized using radio-frequency (RF) transport measurements for frequencies between 0.03 and 40 GHz using a variable network analyzer, in a cryogenic RF-probe station, as detailed in our previous works.[31,34,35] The S-matrix components are extracted by measuring the reflected and transmitted wave intensity through the device as a function of frequency for different gate voltages using a variable network analyzer. The complex admittance (inverse impedance) is then extracted from the S-matrix components. The real and imaginary parts of device admittance are quantified versus frequency and gate voltage. Proper care is taken to de-embed parasitic capacitive and inductive contributions resulting from the device geometry by measuring a dummy device having identical contact geometry

without the Bi_2Se_3 flake in between, as well as a conductive through-line. All measurements are made at 10K.

Results

Sample characterization

An optical microscope image of a characteristic sample is shown in Fig. 2(b,c), before and after the CVD growth of Bi_2S_3. A layer of Bi_2Se_3 is seen to coat the hBN flakes, but does not-nucleate on the SiO_2. A Z-contrast scanning electron microscope image shown in Fig. 1(d) confirms nucleation of Bi_2Se_3 on the hBN flake. This consistent with previous reports on similar growth procedures to synthesize Bi-based TI on hBN using CVD.[36,37]

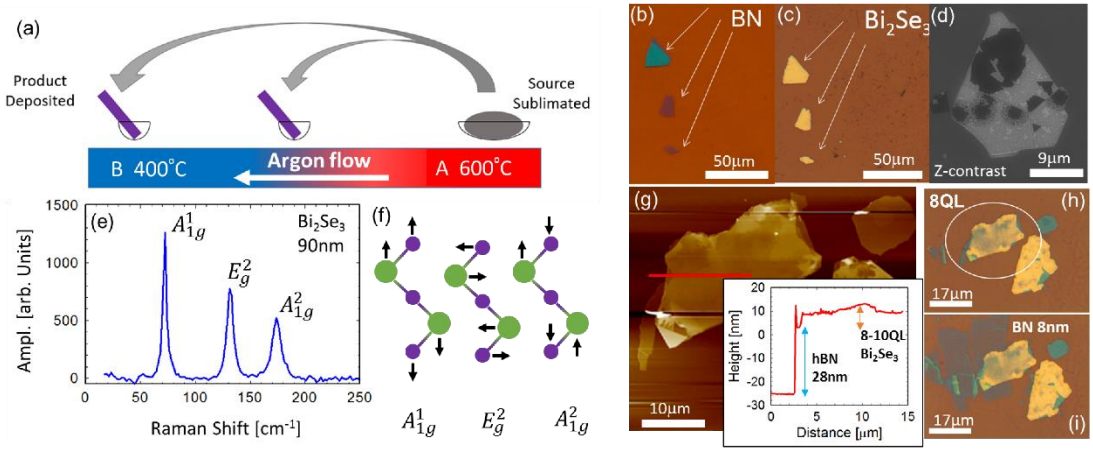

Figure 1. (a) Schematic of CVD growth tube showing Bi_2Se_3 source in hot zone A, and substrates in colder zone B, down stream in the Argon flow direction. (b) Optical microscopy image showing hBN exfoliated flakes on SiO_2 prior to growth. (c) The same hBN flakes coated with Bi_2Se_3 after the growth. (d) Z-contrast SEM image of Bi_2Se_3 growth (dark patches) on hBN. (e) Microscopic Raman spectroscopy on a 90nm thick Bi_2Se_3 flake grown on hBN showing three Raman active peaks corresponding to the three vibrational modes shown in (f), namely, the A_{1g}^1 and A_{1g}^2 out-of-plane modes and the E_g^2 in-plane mode. (g) AFM image of a selected 8QL thick Bi_2Se_3 flake. Inset shows the height as a function of distance measured along the yellow line shown in the picture. The Bi_2Se_3 is 8-10QL thick, and the underlying hBN is 28nm thick. (h) Optical microscope image of the flake shown in (g). (i) 10QL Bi_2Se_3 flake with an 8nm hBN flake transferred on top using the dry-transfer method.

Fig. 1(d) shows a Raman spectrum obtained on the large Bi_2Se_3 flake shown in Fig. 1(e). Three characteristic Raman active phonon peaks (Fig. 1(f)) are observed between 50 and 200 cm^{-1}, confirming the presence of a Bi_2Se_3 layer on the exfoliated hBN. A thinner flake obtained from an identical growth is selected and studied using AFM. This is shown in Fig. 1(g). We first measure the Bi_2Se_3 thickness across a line shown in the inset of Fig. 1(g). We find a thickness varying between 8 and 10 quintuple layers (QL) considering a small observed surface roughness of 1QL.

A top hBN flake is then transferred on top of the grown Bi_2Se_3 using the standard dry transfer method already proven successful for graphene[40,41] and 2D semiconductors.[42,43,44] Optical images of the samples are shown in Fig. 1(h, i) before and after the transfer respectively. The transfer is performed in air, therefore exposing the top surface of the Bi_2Se_3 flake to atmospheric conditions. The transferred hBN layer is chosen to be thinner than 10 nm (8 nm in this case), in order to maximize the geometric capacitance due to the hBN and render the quantum capacitance of the Bi_2Se_3 experimentally visible. A Ti(5 nm)/Au(150 nm) contact is deposited using e-beam evaporation to connect the source electrode to

Bi_2Se_3. Light argon etching (<10 s) is performed in-situ to remove any native oxides, before the contact is deposited. The hBN-encapsulated Bi_2Se_3 capacitor is then embedded in an RF-waveguide Fig. 2 (a, b). The waveguide, the source electrode and the gate electrode are all deposited simultaneously.

RF-transport measurements

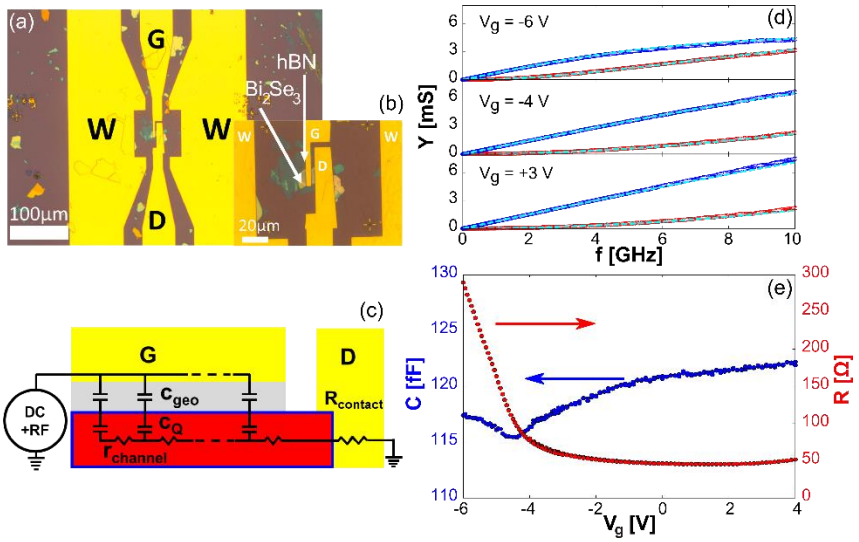

Figure 2. (a) Optical microscope image of the finished device with the capacitor shown embedded inside a coplanar waveguide (W). G and D denote the gate and drain contacts respectively. (b) Zoomed in microscope image showing the capacitor device. (c) Real and Imaginary parts of the RF-admittance as a function of frequency for three typical gate voltages. (d) Schematic of a distributed RC-line model in series with a contact resistance. The capacitance is split into two components the geometric capacitance C_{geo} and the quantum capacitance C_Q. (e) Total device capacitance and channel resistance extracted by fitting the model corresponding to the circuit shown to the data shown in (c). Curve fits in (c) are shown as solid lines.

The de-embedded sample admittance versus frequency is shown in Fig. 2 (c) for three different gate voltages. The real part is shown in red and the imaginary part in blue. The data is then fit using a distributed RC-line model (of admittance Y_{RC}) in series with a contact resistance $R_{contact}$, similar to what was previously reported for graphene (Fig. 2(d)) [31]. The total admittance Y_{total} is given by:

$$Y_{total}(\omega) = \frac{1}{Y_{RC}^{-1}(\omega) + R_{contact}}, \qquad (1)$$

where

$$Y_{RC} = j\omega CLW \frac{\tanh(L\sqrt{j\omega C}/\sigma)}{L\sqrt{j\omega C}/\sigma} \qquad (2)$$

Here, $\omega = 2\pi f$ is the frequency, $j = \sqrt{-1}$ and $L = 4.3\mu m$ and $W = 12.8\mu m$ are the device length and width, respectively. σ is the channel conductivity. C is the total device capacitance:

$$C^{-1} = c_{geo}^{-1} + c_Q^{-1} \qquad (3)$$

Where c_{geo} is the geometric capacitance and $c_Q = e^2\chi$ is quantum capacitance related to the compressibility $\chi = \frac{\partial n}{\partial \varepsilon_F}$. Here ε_F represents the chemical potential at the sample surface and n is the 2D sheet carrier density.

The curve fit of $Y_{total}(\omega)$ allows us to separate C and σ for different gate voltages. As seen in Fig. 2(c), the model yields an excellent fit to the data up to 10 GHz. The validity of the model has also been confirmed up to 40 GHz from which we deduce an estimate of the access resistance on the order of 20 Ω. Results for C and R from curve fits up to 10 GHz are shown in Fig. 2(e) a function of gate voltage between -6 V and 1V. The capacitance decreases progressively for decreasing voltage (0 to -6 V), goes through a minimum at about -5 V, then increases again between -5 V and -6 V. With a capacitance dip of 5%, our results confirm previous low frequency capacitance measurements on similar Bi_2Se_3 reporting on a capacitance dip of 6%.[36] We show below that the quantum capacitance background at the dip is due to a strong contribution of the bottom layer which is a hallmark of high quality Bi_2Se_3 crystals.

The resistance exhibits a continuous increase that accelerates near the capacitance minimum. No resistance maximum is observed. A fixed contact resistance $R_c \approx 20\Omega$ was included in the curve fit to the admittance data. Allowing this contact resistance to vary yielded negligible variation compared to the 5-fold increased observed in the channel resistance. We can thus confidently claim, that our two-point RF measurements yields a reliable simultaneous measurement of the quantum capacitance and the channel resistance.

Analysis of the quantum capacitance

We next focus on the analysis of quantum capacitance. c_Q can be extracted using Eq. (3), by fixing $c_{geo} = (124 \pm 1)$ fF, the value at which the capacitance is seen to saturate in Fig 2(d). The measured geometric capacitance is slightly lower than what is expected for hBN having κ=3.2, possibly as a result of the rough surface of Bi_2Se_3. The capacitance per unit area c_Q is then determined by dividing the capacitance by the geometrical factors *L* and *W*. c_Q is shown in Fig. 3 (a). The shaded grey area in Fig. 3(a) is the propagated uncertainty on c_Q due to the uncertainty associated with c_{geo}. A powerful consequence of our measurements is the fact that it allows us to determine the local (top surface) chemical potential ε_f directly from experimental data via the Berglund integral, without a priori knowledge of the band structure. The Berglund integral is written as[45]:

$$\varepsilon_f = \int_0^{V_g} dV \left(1 - \frac{C(V)}{c_{geo}}\right) \qquad (4)$$

We use Eq. (4) to extract ε_f which we now plot as a function of V_g in Fig. 3(b) along with the propagated uncertainty associated with it. We can now plot the quantum capacitance c_Q versus the local chemical potential ε_f. This is shown in Fig. 3(c). The minimum in c_Q defines the chemical potential origin, as it is associated with the position of the Dirac point. This allows us to determine the Fermi energy at zero

applied potential to be close to 200 meV above the Dirac point. This corresponds to a surface Dirac carrier density of 3.0×10^{12}cm^{-2}. Assuming the Dirac point occurs at the center of the energy gap at 150 meV below the bottom of the conduction, this also corresponds to a Fermi level position close to 50 meV above the conduction band bottom. This yields a slight native bulk n-doping of 4.0×10^{18}cm^{-3}. This is a significant improvement compared to pristine quality Bi_2Se_3 where typically $n > 10^{19} cm^{-3}$ [22,46,47,48] and agrees with previous reports on improved quality samples.[26]

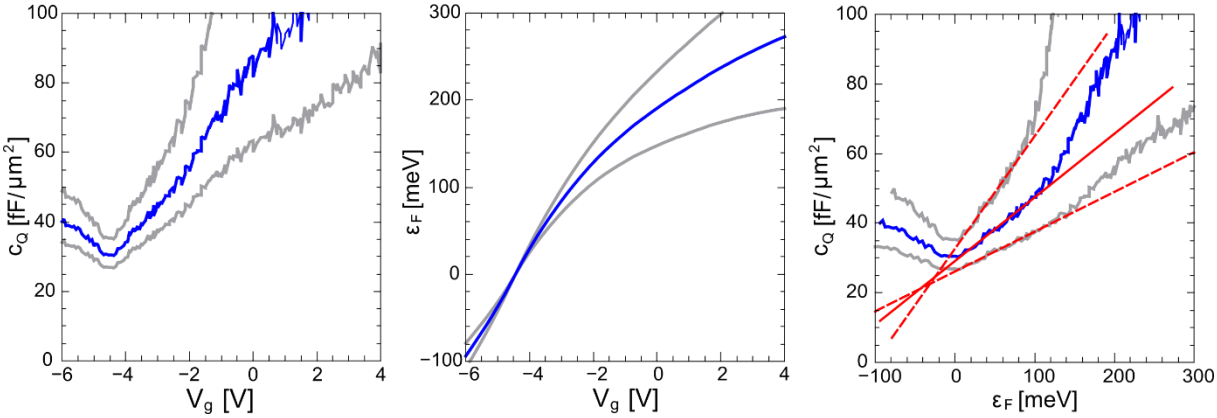

Figure 3. (a) Quantum capacitance versus gate voltage at 10K. (b) Surface chemical potential (Fermi energy) versus gate voltage. (c) Quantum capacitance versus Fermi energy. Blue line represents data, grey lines show uncertainty extrema, red lines are linear fits using Eq. 5.

We can additionally perform a linear fit to the c_Q versus ε_f curve. This is shown as the solid red line, fit to the data. The dashed lines are fit extrema to the edges of the shaded area, and allow us to determine the uncertainty on the extracted slope. The slope allows us to extract the Dirac velocity of the topological surface states, near of the Dirac point. This follows from the expression of the compressibility χ, which is related to c_Q:

$$c_Q = e^2\chi = \frac{e^2\varepsilon_f}{2\pi(\hbar v_f)^2} \quad (5)$$

We find a Dirac velocity equal to $(5.8\pm1.4)\times10^5$m/s. This agrees within experimental uncertainty with previously reported velocities that vary between 5×10^5m/s and 4.5×10^5m/s.[14,15,18] Before moving in to the analysis of the resistance data, it is worthwhile highlighting that while we can perfectly account for variation of the quantum capacitance versus Fermi energy shown in Fig. 3(c), this simplified analysis cannot account for the finite c_Q offset observed at the minimum. From Eq. (5) it is evident that c_Q should go to zero at $\varepsilon_f = 0$. Although this has never been observed experimentally, the typical capacitance offset at the Dirac point observed in graphene for example is an order of magnitude lower than what is observed here.[49] A thorough understanding of the capacitive contributions of other transport channels must thus be provided.

Two models are considered next to address this problem in Fig. 4(a-c). Model (I) treats the case of a fully depleted insulating bulk that contributes a geometric, between two metallic surfaces. In model (II), populated bulk bands contributes a quantum capacitance, related to surface charge accumulation or depletion that screens the electric over a finite length. We shall demonstrate next, that close to the capacitance minimum, Model (I) can quantitatively explain the variation of the quantum capacitance with the chemical potential. Far away from the minimum, we will use model (II) to estimate the screening length. We will show that in sufficiently thin Bi_2Se_3 flakes, the electric field can penetrate the

entire sample thickness, when the chemical potential is close to the conduction band edge. This allows a full depletion of the bulk bands and confirms the validity of model (I) near the capacitance minimum.

Capacitance model (I) is summarized by the circuit shown in Fig. 4(b). Essentially, in the bulk depleted regime, the top surface is directly coupled to the gate via the dielectric's geometrical capacitance c_{geo}. The bottom TSS is however coupled via an additional geometrical capacitance that is due to the insulating bulk of Bi_2Se_3 as shown in Fig. 4(b). Overall the total quantum capacitance corresponding to this circuit is given by:

$$c_Q = c_Q^{TTSS}(\varepsilon_f) + \left(\frac{1}{c_g^{Bulk}} + \frac{1}{c_Q^{BTSS}(\varepsilon_f)}\right)^{-1} \quad (6)$$

The quantum capacitance of the top TSS c_Q^{TTSS} is computed using Eq. (5), with $v_f \approx 5\times10^5 m/s$.[18] Note that here ε_f is the top surface chemical potential. Hence, the expression for that of the bottom TSS $c_Q^{BTSS}(\varepsilon_f)$is not simply given by Eq. (5). We show in the supplement, that effective capacitance of the bottom TSS that is capacitively coupled via the insulating bulk is given by:

$$\left(\frac{1}{c_g^{Bulk}} + \frac{1}{c_Q^{BTSS}(\varepsilon_f)}\right)^{-1} = c_g^{Bulk}\left[1 - \frac{1}{\left(\sqrt{1 + \frac{e^2|\varepsilon_F + W|}{2\pi(\hbar v_f)^2 c_g^{Bulk}}}\right)}\right] \quad (7)$$

W is the band offset between the top and bottom TSS. It is the only adjustable parameter in the model. The geometric capacitance of the insulating bulk can calculated using:

$$c_g^{Bulk} = \frac{\kappa\varepsilon_0}{d_{Bi2Se3}} \quad (8)$$

where, $\kappa \approx 100$[29,50,51,52,53] is the generally accepted static dielectric constant of Bi_2Se_3. $\varepsilon_0 = 8.85\times10^{-12} F/m$ is the permittivity of free space, and $d_{Bi2Se3} \approx 8\ nm$ is the thickness of Bi_2Se_3 flake. We thus find $c_g^{Bulk} \approx 110$ fF/μm^2 which is much larger than the quantum capacitances of the surface states, indicating a strong electrostatic coupling between top and bottom surfaces and an almost flat electrostatic potential within the bulk. The contribution of c_Q^{TTSS} is shown in red in Fig. 4(a). The evolution of the effective capacitance of the bottom TSS c_Q^{BTSS} in series with insulating bulk as a function of top-surface chemical potential ε_f is shown in magenta.

We find that W ≈ 140 meV yields a good agreement between the data and Eq. (6) and (7), as seen in Fig. 4(a). We observe that the effective quantum capacitance associated to the bottom surface flattens out at large values of ε_f. This is due to an enhanced screening of the electric field at large charge carrier density by the top-TSS. We have thus shown that the measured quantum capacitance can be reliably explained by a model of two capacitively coupled TSS. This model accounts for the different slopes measured away from the minimum, and explains the offset observed at the minimum. Such a strong bottom-TSS contribution to compressibility has been disregarded in HgTe samples studied previously.[35,54] It becomes important here due to the large permittivity, the large band gap and the nanometer thickness of the Bi_2Se_3 crystals grown by CVD. Importantly, for a top-surface chemical potentials ε_F between 0 and -140 meV, the top and bottom surface have different carrier polarity, i.e. p-type and n-type, respectively.

Far away from the capacitance minimum, bulk bands are filled. In this situation, one has to take into account the effect of bulk screening (model (II) shown in Fig. 4(c)). In this situation, a semi-infinite bulk model that includes a top TSS can be used. The details of the screening model are shown in the appendix.

However, it is useful to note that near the bulk band edge, when the quantum capacitance from bulk carriers becomes small, one can show that the screening length increases according to:

$$\lambda = \frac{\kappa \varepsilon_0}{c_Q^{bulk}} \qquad (9)$$

For $c_Q^{bulk} < 110$ fF/µm², λ exceeds 8 nm, the thickness of the sample, implying full bulk depletion (detailed in supplement). In Fig. 4(a), this corresponds to a Fermi energy of at least 180 meV. Below this Fermi energy, the field effect is therefore able to fully deplete the bulk and model (I) holds, alternatively model (II) would start dominating above 180 meV. Our determination of the quantum capacitance is not accurate enough in this range. We are thus unable to make a quantitative analysis of the crossover from regime (I) to (II).

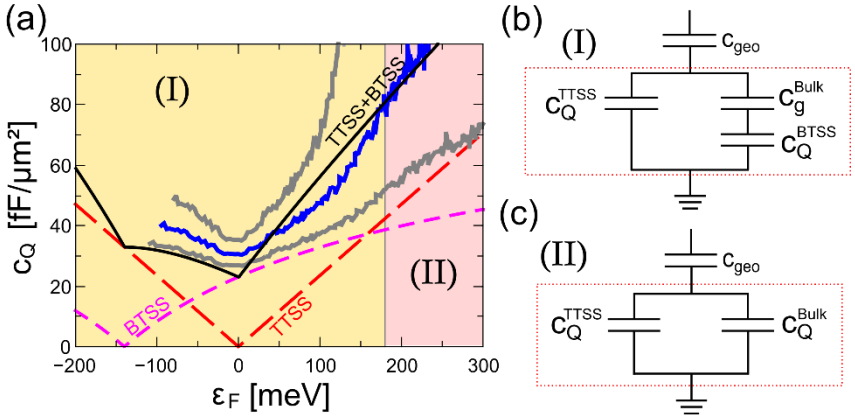

Figure 4. (a) Quantum capacitance versus surface chemical potential data (blue) compared to model of topological insulator shown in (b). Gray curves represent upper and lower bounds of experimental data, black solid is the total quantum capacitance resulting from this model, dashed red line in that of the top TSS, dashed magenta line is that of the bottom TSS. (b) MITI-CAP model of a topological insulator in the bulk depleted regime where the top TSS (c_Q^{TTSS}) is capacitively coupled to the bottom TSS (c_Q^{BTSS}) via the insulating bulk assumed to have a geometrical capacitance (c_g^{Bulk}). (c) Model of a semi-infinite topological insulator in the doped bulk regime, where both the top TSS and the bulk bands (c_Q^{Bulk}) contribute to the quantum capacitance.

Next, we qualitatively discuss the variation of the channel resistance. Near the capacitance minimum, a fast increase of the channel resistance is observed, likely corresponding to the depletion of surface carriers on the top and bottom surface, but no resistance maximum is reached. Since the Fermi energy is likely higher above the Dirac point at the bottom surface, bottom Dirac electrons provide a parallel conduction channel that has a much lower resistivity. The effective resistance from both top and bottom parallel channels is hence dominated by the resistivity of the bottom channel. One does not therefore expect to observe an ambipolar resistance maximum as long as the bottom Dirac cone remains heavily occupied. Lastly, going up in Fermi energy away from the capacitance minimum, the resistance curve flattens out and eventually increases at large positive values of V_g (hardly visible in Fig. 2 (e)). We point out, that this increased scattering at high charge carrier density in top TSS is likely associated to sub-band scattering as reported in Ref.[34,35]. It is worth noting that any issue with the contact resistance can be ruled out. First, the Au/Bi_2Se_3 interface is not under the gate stack and therefore remains ohmic throughout the entire experiment, since Bi_2Se_3 remains n-doped away from the gate stack. Second, even when the top surface is very close to neutrality, the bottom surface of the sample remains carrier doped, thus ensuring a good connection with the source contact. This highlights the strength of our measurement and the local nature of the quantum capacitance in our experiment.

Discussion

Finally, we discuss how our results and our model compare with previous studies on the subject. Our model is similar to what was proposed by Fatemi et al. [20] in the depletion regime to interpret electrostatic

coupling between the top and bottom surface. In ref.[20], a geometric bulk capacitance is estimated for $Bi_{1.5}Sb_{0.5}Te_{1.7}Se_{1.3}$ and yields a dielectric constant of κ=32. This bulk capacitance couples the bottom surface to the applied electric field, and allows a finite band offset between the top and bottom TSS. The depletion regime in Bi_2Se_3 was investigated in ref. [33]. However, only a qualitative analysis of the compressibility of the TSS was performed in this work. Thus, overall, our work bridges the gap between ambipolar DC resistance measurements on gated TIs and low frequency AC measurements on TI capacitors and unifies our understanding of the electrostatic charging curve of TIs in the depletion regime, as summarized by Fig. 4(a,b). It highlights the interest to study Bi_2Se_3 and other Bi-based TIs that can uniquely be grown in the form of thin nanoflakes on hBN. This fact, combined with the large dielectric constant and wide energy gap of Bi_2Se_3, turns out to be essential in allowing one to gate tune these topological materials to the bulk depleted regime, and fully manipulate the Dirac states.

Conclusion

In conclusion, we have performed and analyzed capacitance and transport in the RF regime in Bi_2Se_3 flakes grown by CVD on hBN. The reduced electron doping of Bi_2Se_3 grown in these conditions allows – for the first time – to quantitatively determine the quantum capacitance in Bi_2Se_3 and observe its minimum resulting from the top topological surface Dirac point. A detailed analysis of the field effect mechanism in thin Bi_2Se_3 flakes shows that a bulk depleted regime can be reached at an accessible gate voltage in hBN-encapsulated Bi_2Se_3 allowing to investigate Dirac physics in Bi_2Se_3. A pure surface transport regime is obtained, it is shown that the top and bottom topological surface Dirac cones are likely to be shifted in energy, and are strongly coupled via the insulating bulk. This results in a clearly resolved Dirac point minimum from the top TSS, in the RF quantum capacitance. As an outlook, a dual-gated device might allow to electrostatically compensate the chemical doping asymmetry between the two surfaces. Overall, our work establishes hBN encapsulated Bi_2Se_3 as a promising platform to study Bi-based 3D-TI and motivates future work on their implementation in high frequency transistors, and other RF devices.

Acknowledgement

We acknowledge Michael Rosticher's valuable assistance with cleanroom equipment and the Pascal Morfin for his assistance with growth equipment setup. BAA and JD acknowledge funding from ANR-LabEx grant ENS-ICFP ANR-10-LABX-0010/ANR-10-IDEX-0001-02PSL. JD is partially supported by the Northeastern University Coop fellowship. The scanning electron microscope (SEM) facility of the Institut de Minéralogie et de Physique des Milieux Condensés is supported by Région Ile-de-France grant SESAME 2006 N°I-07-593/R, INSU-CNRS, INP-CNRS, University Pierre et Marie Curie – Paris 6, and by the French National Research Agency (ANR) grant no. ANR-07-BLAN-0124-01. Growth of hexagonal boron nitride crystals was supported by the Elemental Strategy Initiative conducted by the MEXT, Japan and JSPS KAKENHI Grant Numbers JP15K21722.

1. Haldane, F. D. M. Model for a Quantum Hall Effect without Landau Levels: Condensed-Matter Realization of the 'Parity Anomaly'. *Phys. Rev. Lett.* **61,** 2015–2018 (1988).

2. Niu, Q., Thouless, D. J. & Wu, Y. S. Quantized Hall conductance as a topological invariant. *Phys. Rev. B* **31,** 3372–3377 (1985).

3. Kane, C. L. & Mele, E. J. Quantum Spin Hall Effect in Graphene. *Phys. Rev. Lett.* **95,** 226801 (2005).

4. Bernevig, B. A., Hughes, T. L. & Zhang, S.-C. Quantum Spin Hall Effect and Topological Phase Transition in HgTe Quantum Wells. *Science.* **314,** 1757–1761 (2006).

5. Hasan, M. Z. & Kane, C. L. Colloquium: Topological insulators. *Rev. Mod. Phys.* **82,** 3045–3067 (2010).

6. Qi, X.-L. & Zhang, S.-C. Topological insulators and superconductors. *Rev. Mod. Phys.* **83,** 1057–1110 (2011).

7. Ando, Y. Topological insulator materials. *J. Phys. Soc. Japan* **82,** 102001 (2013).

8. Ando, Y. & Fu, L. Topological Crystalline Insulators and Topological Superconductors : From Concepts to Materials. *Annu. Rev. Condens. Matter Phys.* **6,** 361–381

9. Chang, C.-Z. *et al.* High-precision realization of robust quantum anomalous Hall state in a hard ferromagnetic topological insulator. *Nat Mater* **14,** 473–477 (2015).

10. Chang, C.-Z. *et al.* Experimental observation of the quantum anomalous Hall effect in a magnetic topological insulator. *Science.* **340,** 167–70 (2013).

11. Bocquillon, E. *et al.* Gapless Andreev bound states in the quantum spin Hall insulator HgTe. *Nat. Nanotechnol.* **12,** 134–134 (2016).

12. Wu, L. *et al.* Quantized Faraday and Kerr rotation and axion electrodynamics of a 3D topological insulator. *Science.* **354,** 1124–1127 (2016).

13. Shuvaev, A., Dziom, V., Kvon, Z. D., Mikhailov, N. N. & Pimenov, A. Universal Faraday Rotation in HgTe Wells with Critical Thickness. *Phys. Rev. Lett.* **117,** 117401 (2016).

14. Xia, Y. *et al.* Observation of a large-gap topological-insulator class with a single Dirac cone on the surface. *Nat Phys* **5,** 398–402 (2009).

15. Hsieh, D. *et al.* A tunable topological insulator in the spin helical Dirac transport regime. *Nature* **460,** 1101–5 (2009).

16. Analytis, J. G. *et al.* Bulk Fermi surface coexistence with Dirac surface state in Bi2Se3 : A comparison of photoemission. *Phys. Rev. B* **81,** 205407 (2010).

17. Neupane, M. *et al.* Observation of quantum-tunnelling-modulated spin texture in ultrathin topological insulator Bi2Se3 films. *Nat. Commun.* **5,** 3841 (2014).

18. He, K. *et al.* Crossover of the three-dimensional topological insulator Bi2Se3 to the two-dimensional limit. *Nat. Phys.* **6,** 584–588 (2010).

19. Cheng, P. *et al.* Landau Quantization of Topological Surface States in Bi2Se3. *Phys. Rev. Lett.* **105,** 76801 (2010).

20. Fatemi, V. *et al.* Electrostatic Coupling between Two Surfaces of a Topological Insulator Nanodevice. *Phys. Rev. Lett.* **113,** 206801 (2014).

21. Wei, P. *et al.* Exchange-Coupling-Induced Symmetry Breaking in Topological Insulators. *Phys. Rev. Lett.* **110,** 186807 (2013).

22. Taskin, A. A., Sasaki, S., Segawa, K. & Ando, Y. Manifestation of Topological Protection in Transport Properties of Epitaxial Bi2Se3 Thin Films. *Phys. Rev. Lett.* **109,** 66803 (2012).

23. Assaf, B. A. *et al.* Quantum coherent transport in SnTe topological crystalline insulator thin films. *Appl. Phys. Lett.* **105,** 102108 (2014).

24. Dufouleur, J. *et al.* Quasiballistic Transport of Dirac Fermions in a Bi2Se3 Nanowire. *Phys. Rev. Lett.* **110,** 186806 (2013).

25. Veyrat, L. *et al.* Band Bending Inversion in Bi2Se3 Nanostructures. *Nano Lett.* **15,** 7503–7507

(2015).

26. Liu, H., Liu, S., Yi, Y., He, H. & Wang, J. Shubnikov–de Haas oscillations in n and p type Bi 2 Se 3 flakes. *2D Mater.* **2,** 45002 (2015).

27. Yan, Y. *et al.* Synthesis and quantum transport properties of Bi_2Se_3 topological insulator nanostructures. *Sci. Rep.* **3,** 1264 (2013).

28. Qu, D.-X., Hor, Y. S., Xiong, J., Cava, R. J. & Ong, N. P. Quantum oscillations and hall anomaly of surface states in the topological insulator Bi2Te3. *Science (80-.).* **329,** 821–4 (2010).

29. Kim, D. *et al.* Surface conduction of topological Dirac electrons in bulk insulating Bi2Se3. *Nat. Phys.* **8,** 460–464 (2012).

30. Xiu, F. *et al.* Quantum Capacitance in Topological Insulators. *Sci. Rep.* **2,** 669 (2012).

31. Pallecchi, E. *et al.* Transport scattering time probed through rf admittance of a graphene capacitor. *Phys. Rev. B* **83,** 125408 (2011).

32. Wilmart, Q. *et al.* Contact gating at GHz frequency in graphene. *Sci. Rep.* **6,** 21085 (2016).

33. Betz, A. C. *et al.* Supercollision cooling in undoped graphene. *Nat. Phys.* **9,** 109–112 (2012).

34. Inhofer, A. Probing AC compressibility of 3D HgTe and Bi2Se3 topological insulators at high electric fields: evidence for massive surface states. (Ecole Normale Supérieure, 2017).

35. Inhofer, A. *et al.* Topological confined massive surface states in strained bulk HgTe probed by RF compressibility. arxiv1704.04045

36. Xu, S. *et al.* van der Waals Epitaxial Growth of Atomically Thin Bi 2 Se 3 and Thickness-Dependent Topological Phase Transition. *Nano Lett.* **15,** 2645–2651 (2015).

37. Gehring, P., Gao, B. F., Burghard, M. & Kern, K. Growth of high-mobility Bi 2Te 2Se nanoplatelets on hBN sheets by van der Waals epitaxy. *Nano Lett.* **12,** 5137–5142 (2012).

38. Taniguchi, T. & Watanabe, K. Synthesis of high-purity boron nitride single crystals under high pressure by using Ba–BN solvent. *J. Cryst. Growth* **303,** 525–529 (2007).

39. Dean, C. R. *et al.* Boron nitride substrates for high-quality graphene electronics. *Nat. Nanotechnol.* **5,** 722–726 (2010).

40. Mayorov, A. S. *et al.* Micrometer-Scale Ballistic Transport in Encapsulated Graphene at Room Temperature. *Nano Lett.* **11,** 2396–2399 (2011).

41. Guimarães, M. H. D. *et al.* Controlling Spin Relaxation in Hexagonal BN-Encapsulated Graphene with a Transverse Electric Field. *Phys. Rev. Lett.* **113,** 086602 (2014).

42. Xu, S. *et al.* Universal low-temperature Ohmic contacts for quantum transport in transition metal dichalcogenides. *2D Mater.* **3,** 21007 (2016).

43. Chen, X. *et al.* High-quality sandwiched black phosphorus heterostructure and its quantum oscillations. *Nat. Commun.* **6,** 7315 (2015).

44. Xu, S. *et al.* High-quality BN / WSe 2 / BN heterostructure and its quantum oscillations. *arXiv*1503.08427.

45. Berglund, C. N. Surface states at steam-grown silicon-silicon dioxide interfaces. *IEEE Trans. Electron Devices* **ED-13,** 701–705 (1966).

46. He, H. *et al.* High-field linear magneto-resistance in topological insulator Bi2Se3 thin films.

Appl. Phys. Lett. **100,** 32105 (2012).

47. Wu, L. *et al.* A sudden collapse in the transport lifetime across the topological phase transition in (Bi1−xInx)2Se3. *Nat. Phys.* **9,** 410–414 (2013).

48. Son, J. *et al.* Conductance modulation in topological insulator Bi2Se 3 thin films with ionic liquid gating. *Appl. Phys. Lett.* **103,** 213114 (2013).

49. Yu, G. L. *et al.* Interaction phenomena in graphene seen through quantum capacitance. *Proc. Natl. Acad. Sci. U. S. A.* **110,** 3282–6 (2013).

50. Bianchi, M. *et al.* Coexistence of the topological state and a two-dimensional electron gas on the surface of Bi(2)Se(3). *Nat. Commun.* **1,** 128 (2010).

51. Butch, N. P. *et al.* Strong surface scattering in ultrahigh-mobility Bi2Se3 topological insulator crystals. *Phys. Rev. B* **81,** 241301 (2010).

52. Köhler, H. & Becker, C. R. Optically Active Lattice Vibrations in Bi2Se3. *Phys. status solidi* **61,** 533–537 (1974).

53. Park, J. Y. *et al.* Molecular beam epitaxial growth and electronic transport properties of high quality topological insulator Bi 2 Se 3 thin films on hexagonal boron nitride. *2D Mater.* **3,** 35029 (2016).

54. Kozlov, D. A. *et al.* Probing Quantum Capacitance in a 3D Topological Insulator. *Phys. Rev. Lett.* **116,** 166802 (2016).